JAAS
Journal of Analytical Atomic Spectrometry

Accepted Manuscript

This article can be cited before page numbers have been issued, to do this please use: M. Wang, C. Faulmann, C. Hole, F. Wang, C. Luo, T. Wang and P. Sciau, *J. Anal. At. Spectrom.*, 2026, DOI: 10.1039/D6JA00035E.

ROYAL SOCIETY OF CHEMISTRY

rsc.li/jaas

View Article Online
DOI: 10.1039/D6JA00035E

Fe speciation in multiphase assemblages of black and white porcelain (Jin dynasty 1115-1234 CE) using micro-X-ray Absorption spectroscopy

Minli Wang,[1] Christophe Faulmann,[1] Clément Hole,[2] Fen Wang,[3] Chenchen Luo, [1] Tian Wang,[3*] and Philippe Sciau[1,3*]

[1] CEMES, CNRS, Toulouse University, 29 rue Jeanne Marvig, Toulouse 31055, France

[2] ESRF, The European Synchrotron, 71 Avenue des Martyrs, CS40220, 38043 Grenoble Cedex 9, France

[3] School of Conservation Science & Technology for Cultural Heritage, School of Material Science and Engineering, Key Laboratory of Materials & Technology for Underground Cultural Heritage Conservation, Ministry of Education, Shaanxi University of Science and Technology, Xi'an 710021, China

Abstract: Black and white porcelain is a highly heterogeneous multilayer ceramic system, whose technological information and microstructure are influenced by the raw materials composition and complex reactions that occur during the firing process. This study performed several synchrotron radiation-based analytical techniques (μ-XRF mapping, μ-XANES spectra, μ-XANES mapping, and SIXES) to analyze the spatial distribution of major elements in the stratigraphic layers, as well as the spatial distribution of iron speciation. The results show that the pigment sources are diverse, including iron-rich glazes, iron-bearing clay minerals, and non-clay iron minerals. Pigment particles, mainly composed of hematite, play a key role in the formation of decorations. In addition, the valence state of iron among layers is not stable and even exhibits differences at the micrometre scale. Our results also indicate that the multi-technique approaches based on synchrotron-radiation have significant advantages on studying complex layered ceramic systems, especially the μ-XANES mapping and SIXES techniques, which provide information on iron species and their local variations while maintaining micrometre scale spatial resolution.

View Article Online
DOI: 10.1039/D6JA00035E

Key words: black and white porcelain; Iron speciation; μ-XRF mapping; μ-XANES mapping；XANES imaging

1 Introduction

Complex, layered and chemically heterogeneous systems, such as glazed ceramics, typically contain reaction at interfaces, diffusion fronts and redox gradients that occur over length scales from only a few to several hundred micrometers. Elucidating these processes requires analytical methods that can map elemental distributions and determine oxidation states in complex multiphase assemblages. Conventional laboratory analytical approaches often lack the spatial resolution or chemical sensitivity required to capture these subtle changes, especially when multiple crystalline phases coexist with glassy components. Therefore, the mechanisms that control the phase formations and transformations of such composite materials remain incompletely understood.

Black and white porcelain is a type of decorative porcelain with a complex, heterogeneous, multilayered structure, which was produced on a large scale in northern China during the Jin dynasty (1115-1234 CE). Its typical cross-section consists, from the inner layers to the outer ones, of a coarse ceramic body formed from clay-based raw materials, covered with a thin layer of white slip usually prepared from high quality kaolinitic clay, sometimes referred to as “makeup clay” [1–3]. On top of it, a black decoration is added using layers of Fe-based pigments derived from various sources, most commonly Fe-bearing minerals such as magnetite (Fe_3O_4), hematite (α-Fe_2O_3) and goethite (α-FeOOH) [4,5], and of transparent glazes, producing a strong contrast between the black patterns and the white background. In contrast to monochrome ceramics, which typically comprise a relatively simple stratigraphy of body, slip, and glaze, black and white ceramics exhibit a more complex multilayered structure due to the presence of an additional iron-rich pigment layer. This configuration introduces multiple reaction interfaces and heterogeneous sources of iron, thereby promoting coupled processes of dissolution, diffusion, and recrystallization during firing. Due to differences in raw material resource availability and technological development, workshops in different areas

View Article Online
DOI: 10.1039/D6JA00035E

gradually developed distinct production techniques and decorative styles. Therefore, the stratigraphy of the pigmented and non-pigmented layers, and the interactions between the layers during firing, the microstructure and optical properties of black and white porcelain are extremely sensitive to the nature to the raw materials used, pigment preparation and firing conditions.

In recent years, researchers gradually paid more attention to how black and white porcelain was produced. During the manufacturing process, and more specifically during the high temperature steps of the firing, the iron-based crystals undergo profound transformations. Various dissolution and recrystallization processes occur both during the heating and cooling steps leading to modifications of the valence state and the distribution of iron ions especially in the glaze. Furthermore, additional chemical interactions occur at the interfaces, leading to specific crystallizations that can provide key information regarding both the raw materials used and the firing protocol.

The chemical and structural characterization of these thick, multilayer and heterogeneous materials requires at the same time a high spatial resolution over large area. Standard laboratory techniques can provide significant information, such as element composition and its distribution as well as the identification of crystalline phases, but they cannot allow us to study Fe speciation and may lack either the sufficient spatial resolution or field of view. In addition to the crystalline phases containing iron, dissolved ferrous and ferric ions are also present in the glass matrix with a variety of possible coordination environments, such as tetrahedral coordination [6–8], hexa-coordination [9–11], or octahedral coordination [7,12,13]. Therefore, this poses difficulties in revealing the firing process and color-formation mechanism of black and white porcelain.

Synchrotron radiation-based analytical techniques, especially μ-XRF imaging and μ-XANES, are powerful tools for characterizing the stratigraphic distribution of elements and for probing the oxidation states and coordination environments of transition metals at the microscale [14]. In the case of heritage materials, which are highly structured mixtures, several studies have shown the benefit of μ-XAS analyses, which allow to discriminate properly the different layers [6,15–20]. These techniques have been successfully applied to heterogeneous systems such as heritage ceramics from diverse origin,

View Article Online
DOI: 10.1039/D6JA00035E

revealing the evolution of pigment sources [21–24], processing sequences [15,16,18,25,26], and coloring mechanisms [20,27–30]. While μ-XANES point analyses are generally the standard procedure to provide information on oxidation state and coordination of one selected element, Selectively Induced X-ray Emission Spectroscopy (SIXES) allows to obtain the spatial distribution of the chemistry of the targeted element [31]. This approach has been successfully applied, notably in paintings, to explore the chemistry behind pigment degradation [24,32]. In these studies, the targeted elements (S, Cr, Cd) exhibit marked pre-edges and significant differences in XANES spectral features, which make the selection of the energies to obtain a chemical contrast fairly straightforward.

In this study, we demonstrate that SIXES is capable of discriminating between iron species with similar oxidation states at the Fe K-edge, extending its applicability beyond systems characterized by strongly contrasting XANES signatures. When associated to μ-XRF imaging and punctual μ-XANES analysis, SIXES can indeed be a powerful tool for studying the distribution of Fe based phases in the complex layered structure of black and white porcelain with the adequate large field of view. Results provided a crucial insight into the role of Fe both as a proxy of the manufacturing process and as the coloring agent leading to the aesthetic aspects of black decorations. Moreover, it enabled us to uncover key information about production techniques, and to elucidate the optical properties of coloring elements, and shed new light on the raw material selections and firing conditions in black and white porcelain.

2 Experimental details

2.1 Sample description

Seven black and white porcelains produced by private workshops in Shanxi Province are the main focus of this study, together with one black-glazed porcelain (GZ01) that serves as a reference sample. According to stratigraphic and archaeological classification, these samples ware mainly produced during the Jin Dynasty (1115-1234 AD) in Hejin Kilns (GZ-BD01), in Xiangning Kilns (TGD-BD04, TGD-BD06, TGD-BD08, TGD-BD14) and in Huozhou Kilns (HZ-BD01 and HZ-BD02). The sample photos are shown in

View Article Online
DOI: 10.1039/D6JA00035E

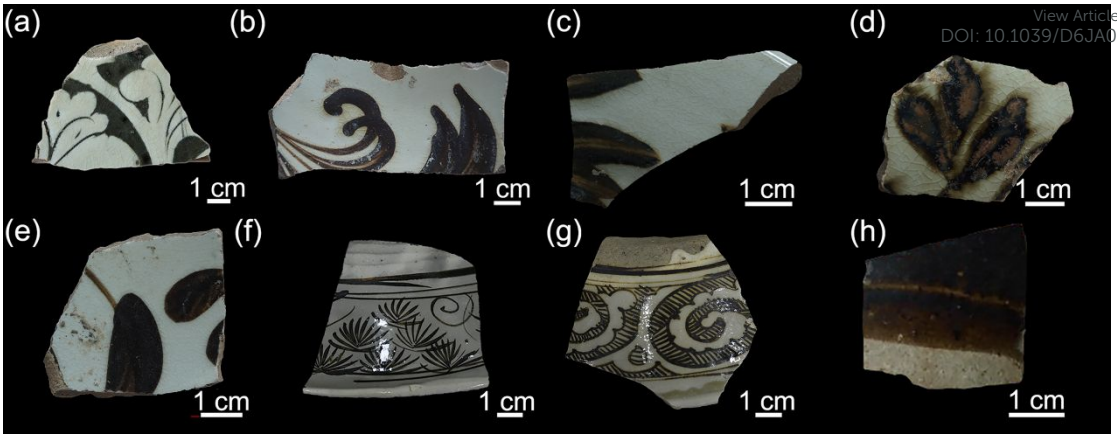

Figure 1. Their common characteristic is that the gray coarse body is covered with a layer of white slide and the glaze and decorative areas are glossy.

2.2 Thin cross-section sample preparations

Since the glaze is thin and layered, it is essential to carefully prepare a thin cross-section of the samples to preserve as much as possible the original stratigraphy of the sample. As such, the preparation method of thin section samples used here is similar to that of transmission microscopy, the detailed sample preparation process can be found in the study by Tian et al [20]. In this study, the final thickness of the samples after polishing was between 40 and 100 μm. The advantage of this preparation approach is that it protects the very superficial layer of glaze from damage and better in-depth information.

2.3 Synchrotron radiation investigations

The synchrotron-based measurements were performed at the ID21 beamline of the European Synchrotron Radiation Facility (ESRF, Grenoble, France). Undulator-generated X-rays were monochromatized using a Si (311) double-crystal monochromator. The beam was focused by Ni-coated Kirkpatrick–Baez mirrors to ~1.0 (h) × 0.7 (v) μm^2 at the sample. Incident intensity (I_0) was monitored with an upstream photodiode, and transmitted intensity with a downstream photodiode for transmission measurements; fluorescence photons were recorded with a silicon drift detector positioned at ~90° to the incident beam. When required, attenuators were added inserted to keep the detector dead-time within the right range. All measurements were performed under vacuum to minimize scattering and air-induced reabsorption of fluorescence and to limit reactions between the metal centre and ambient

View Article Online
DOI: 10.1039/D6JA00035E

gases [33]. Energy calibration used an iron metal foil, with the first inflection point of the Fe K-edge set to 7111.32 eV (corresponding to the maximum of the first-order derivative).

2.3.1 Acquisition of μ-XRF map Images

Two-dimensional μ-XRF maps were acquired by raster-scanning the samples in the vertical mounting geometry, while I_0 was continuously monitored upstream to correct for temporal variations in incident flux. During mapping, attenuators were put in the beam as needed to control flux and maintain the detector dead-time in the desired range (~30%).

2.3.2 Acquisition of μ-XANES spectra

XANES point spectra, collected in both fluorescence and transmission modes, were acquired with a step size of 0.15 eV and dwell time of 0.04s. The spectra were collected through profile lines from the body to the glaze surface to track changes in iron species across the depth of the glazes. Reference spectra of hematite (α-Fe_2O_3), magnetite (Fe_3O_4), wustite (FeO), pseudobrookite (Fe_2TiO_5) and ε-Fe_2O_3 were measured in transmission using an unfocused beam (~300 × 300 μm^2) with a dwell time of 100 ms per point.

2.3.3 Acquisition of μ-XANES mapping and Selectively Induced X-ray Emission Spectroscopy (SIXES) mapping

To further explore the different Fe-species distribution, μ-XRF mapping of areas of interest was implemented at several energies. Depending on the number of energies selected, this hyperspectral approach allows either (i) to fully reconstruct a 2D-XANES map when maps are measured at enough different energies or (ii) to discriminate specific well-defined species by selecting carefully a few characteristic energies. In the rest of this paper, the first case is referred to as μ-XANES mapping, while the second as SIXES mapping.

μ-XANES maps were acquired over areas within the pigmented layers of TGD-BD06 (336 × 178 μm^2) and HZ-BD01 (219 x 126 μm^2). In this case, maps were recorded around the Fe K-edge with energies ranging from 7085 eV to 7240 eV with step size of ~1×1 μm^2. Such acquisition generated hyperspectral images of about 4000 XANES spectra, each pixel corresponding to one spectrum.

View Article Online
DOI: 10.1039/D6JA00035E

SIXES maps are implemented on areas across, the pigmented layers of TGD-BD14 and GZ-BD01. 13 energies were selected by comparing the features of the spectra of reference spectra (7080, 7090, 7100, 7114, 7125, 7131, 7133, 7136, 7146, 7167, 7195, 7240, 7258 eV). Flat-field corrections and image re-alignment was implemented on the different maps. After pre-processing, the maps acquired at different energies were compared to identify the features of the different mineral presents.

2.3.4 Analysis of data

Initial XANES data extraction and preprocessing were performed using in-house scripts. Fe K-edge XANES spectra were then normalized and analyzed in Orange Data Mining software [34]. PCA of the smoothed second derivatives partitioned the spectra into clusters, allowing to average data according the clusters. Pre-edge of the averaged spectra were then fitted. This approach is used because the pre-edge energy and intensity are sensitive to the Fe oxidation state and coordination geometry [7,35]. The pre-edges were fitted using Igor pro software with Gaussian function to obtain the centroid and integrated intensity. Compared them with reference spectra to infer Fe valence and coordination. To improve accuracy, the fitting range was restricted to ~7108-7117 eV following Fiege et al [36], with careful background subtraction to avoid biasing intensities. For estimating $Fe^{3+}/\Sigma Fe$, we considered the two approaches of Wilke et al. [37]—the intensity ratio $I(Fe^{3+})/[I(Fe^{3+})+I(Fe^{2+})]$ and the centroid (C). In line with Cottrell's high-precision calibration for silicate glasses [38], we adopted the centroid method to determine $Fe^{3+}/\Sigma Fe$ in the glass matrix (Eq. 1). It is worth noting that this method is heavily matrix dependent, so this is an approximation and has to be taken with caution.

$$Fe^{3+}/\Sigma Fe \times 100 = \left[-0.028 + \left(0.000784 + 0.00052(7112 - C)\right)^{0.5}\right] \Big/ 0.00026$$

(7112eV≤C≤7113.5eV) (Equation 1)

μ-XANES maps were also analyzed with Orange Data Mining: after image realignment and spectral fitting, spectra were extracted and processed as in the point analyses, using K-means and PCA for clustering. The resulting classes were displayed on a scatter plot, and cluster-averaged spectra were computed to derive the Fe chemistry and valence distributions.

View Article Online
DOI: 10.1039/D6JA00035E

The PyMCA software was used to batch fit the XRF spectra to generate elemental maps (Al, Si, K, Ca, Fe, Ti, Mn), and to normalize those maps to the incident beam intensity [39]. SIXES maps were also visualized by using PyMCA's ROI imaging tool.

3 Results and discussion

3.1 Elemental distribution

Figure 2 shows the elemental distribution of Fe, Al, and Ca in the cross-section of the decorations. Preliminary investigation revealed a large number of anorthite crystals and iron-bearing particles in the pigmented areas of the most samples [40]. These stratigraphies provide important clues regarding the application and raw material used as the pigments. The anorthite-rich layer between pigment and upper glaze layer in GZ-BD01 and TGD-BD04 is consistent with the use of a clay-bearing Fe pigment also rich in Al. The local removal of slip in GZ-BD01 suggests an additional carving or scraping technique. In TGD-BD06, the coexistence of Fe particles with abundant anorthite crystals within the pigment layer revealed that the raw pigment contained Fe-bearing minerals and Ca-bearing component, with less clay. In contrast, TGD-BD08 shows broadly homogeneous Ca and Fe throughout the glaze, implying coloration by Fe-rich glaze rather than an iron-particulate pigment layer. HZ-BD01 and HZ-BD02 display the pigment layer is rich in Fe (only hematite) but without Ca and Al, and there is a slight diffusion of iron into the glaze layer, it suggests that the raw pigments are made of iron-ore dominated pigment without kaolin-based clay, whereas TGD-BD14 is Fe-rich but Al/Ca-poor, indicating the mineral-dominated Fe pigment with minor kaolin/feldspar components. The black-glazed reference GZ-01 differs by showing Fe dispersed in the glaze matrix and anorthite confined near interface between the glaze and body.

3.2 Iron valence and coordination analysis

PCA processing of the μ-XANES point analyses of pigmented areas, as illustrated by the PC1/PC2 scatter plot in Figure S1 (Supporting Information), reveals that samples GZ-BD01, GZ01, TGD-BD04, TGD-BD08 and TGD-BD14 form a single cluster, which suggest a relatively homogeneous chemical environment for Fe in these samples, while points measured on TGD-BD06,

View Article Online
DOI: 10.1039/D6JA00035E

HZ-BD01, and HZ-BD02 each divide in two distinct clusters, indicating heterogeneity in the Fe environments in these cases. It is important to note here that XANES spectra record the average Fe environment in the measured volume, so one spectrum can contain features of both Fe-rich crystallized particles and Fe ions of the glassy matrix. Hence, homogeneous chemical environment does not mean that Fe as one unique chemical environment, but rather several co-existing in a homogeneous manner in the pigmented layer.

The average XANES spectra of clusters are shown in Figure 3. Samples GZ-BD01, GZ01, TGD-BD08, and TGD-BD14 exhibit pre-edge centroid and absorption edge positions similar to those of hematite, confirming the dominance of Fe^{3+} in the pigmented layer. However, their comparatively more intense pre-edge features and broader white lines suggest that Fe^{3+} is located in a lower-symmetry environment, likely associated with disordered crystals or ions in glassy matrices. In contrast, the spectra of TGD-BD04, TGD-BD06_cluster2, HZ-BD01_cluster1, and HZ-BD02_cluster1 closely match the reference hematite spectrum, in agreement with Raman spectroscopy, which confirms the presence of abundant hematite crystals in these regions (Figure S2). It is worth noting that these hematite crystals are not structurally ideal and may exhibit lattice distortions, possibly caused by the high-temperature firing and likely elemental substitution.

The results of the fitting of the pre-edge features of the Fe K-edge spectra recorded on the pigmented area and the upper glassy matrix are shown in Figure 4a and 4b, respectively. The colored solid points represent the samples of this study, the black hollow points represent the reference spectra (hematite, magnetite, wustite, maghemite, and $Fe_2(SO_4)_3$), and the gray circles represent the corresponding centroid and integral intensities of Fe^{2+} and Fe^{3+} in the various geometrical sites of the model compounds obtained by Wike et al. [13,41]. All centroid positions are near ~7113.5 eV, suggesting a predominance of Fe^{3+} in both the pigment and the upper glaze, although some Fe^{2+} is likely present. The pre-edge features of the glaze layer are represented by error bars rather than clustered points due to the variations in the Fe^{3+}/Fe^{2+} ratio within the glaze layers.

In the pigmented area (Figure 4a), the pre-edge features of the spectra corresponding to HZ-BD01_cluster1, HZ-BD02_cluster1, TGD-BD06_cluster1,

View Article Online
DOI: 10.1039/D6JA00035E

and TGD-BD04 closely match the reference hematite, further confirming the presence of hematite crystals. In contrast, the pre-edge features of the other spectra are located between those of the magnetite reference and the $^{[5]}Fe^{3+}$ and $^{[6]}Fe^{3+}$ model compounds from Wilke *et al.* studies [41,42]. Besides, the centroid of the pre-edge in the pigmented area of GZ-01 is located around 7113.0 eV, suggesting a significantly lower Fe^{3+}/ Fe^{2+} ratio.

In the glaze layers (Figure 4b), the integrated intensity of the pre-edge increases compared to the pigmented layer, indicating that the coordination number of iron decreases. According to the model of Wilke *et al.*, it seems to be approaching 5-coordinate in average. Fe^{3+} is usually in a tetrahedral environment in silicate glass [9,43], but high concentrations of alkali and alkaline earth ions may cause Fe^{3+} to switch from a 4-coordinated to a 5-coordinated or even a 6-coordinated environment, which is consistent with the previously discussed results [44].

Table 1 shows the estimated $Fe^{3+}/\Sigma Fe$ ratio of each layer of the stratigraphy calculated using the equation 1 in 2.3.4. The black and white porcelain samples seem dominated by Fe^{3+}, though small amount of Fe^{2+} is present, suggesting that firing atmosphere was more strongly oxidizing. TGD-BD04 exhibits the highest $Fe^{3+}/\Sigma Fe$, suggesting that it was likely fired under the most strongly oxidizing atmosphere among the studied corpus. The $Fe^{3+}/\Sigma Fe$ ratios in each layer of the glazes of TGD-BD08, HZ-BD01, and HZ-BD02 are relatively comparable, indicating that the atmosphere seems stably controlled throughout the whole firing stages. Conversely, GZ-BD01, TGD-BD06, and TGD-BD14 have higher concentrations of Fe^{3+} in the bodies than the other layers, which indicates that the samples were fired in an oxidizing atmosphere during the heating but a slight reduction process may have occurred during the latter stages of heating. Besides, the black glaze GZ-01 exhibits significantly lower $Fe^{3+}/\sum Fe$ ratios in the body (49.7%) and the pigment-containing glaze layer (49.0%) compared to the upper glaze (100%). This distribution suggests that GZ01 may have been fired in a neutral or mildly reducing atmosphere during the heating stage followed by an oxidizing atmosphere during cooling, resulting in complete oxidation of the outer glaze while partial Fe^{2+} was retained in the inner layers [45].

View Article Online
DOI: 10.1039/D6JA00035E

XANES spectra were also acquired as profiles across the stratigraphy of the samples, from the surface to the bottom of the glaze layer in HZ-BD02, TGD-BD04, TGD-BD006 and TGD-BD14. The centroid positions of the Fe pre-edge features are plotted against the corresponding depth in Figure 5. This figure shows that the Fe^{3+}/Fe^{2+} ratio in depth across the glaze are not constant but changes gradually with depth, which is attributed to the diffusion of electronic holes and ions that generate oxidation gradients during firing [46]. In HZ-BD02, TGD-BD04, and TGD-BD14, the centroid position gradually increased with distance from the glaze surface, indicating a gradual increase in Fe^{3+} and a gradual decrease in Fe^{2+}, close to the glaze surface. On the contrary, in TGD-BD06, the centroid position decreases with increasing depth, Fe^{2+} gradually increases and Fe^{3+} gradually decreases.

The valence state of iron in the glass network at the surface of glazes is usually related to the atmosphere conditions during the cooling stage. As such, if the cooling step is done in an atmosphere more oxidizing than the prior, an oxidation gradient should appear with Fe being more oxidized at the surface than deeper. On the contrary, if the cooling stage is more reducing than the prior steps of the firing, Fe should appear more reduced at the surface. Fe appears less oxidized at the surfaces of HZ-BD02, TGD-BD04, and TGD-BD14, which suggest that they may have been exposed to a less oxidizing atmosphere, while the deeper regions experienced stronger oxidation. In contrast, TGD-BD06 shows the reverse trend, so this sample was likely exposed to a more oxidizing atmosphere. The more $Fe^{3+}/\Sigma Fe$ in the bodies indicates that they experienced more oxidizing process (Table 1). During firing, the combustion of organic components in the body and white slip, as well as the calcination of minerals (such as carbonates), leads to an increase in open porosity [47]. The expanded pore network promotes the diffusion of oxygen into the pigment and glaze layers, thereby further promoting the oxidation of iron ions. Therefore, the $Fe^{3+}/\Sigma Fe$ ratio in the pigmented and glaze layers may be influenced by both the external firing atmosphere and oxygen diffusing upward from the bodies.

Figure 6 shows μ-XANES maps and XANES spectra of the pigmented areas of HZ-BD01 (a-d) and TGD-BD06 (e-h). Figure 6a and 6e are the maps of edge jump, this is correlated to the concentration of Fe (red area is enrich

View Article Online
DOI: 10.1039/D6JA00035E

in Fe). Figure 6b and 6f are the Fe valence state maps, red areas contain higher Fe^{3+}, while blue areas contain less Fe^{3+} but more Fe^{2+}. Figure 6c and 6g show the spatial map of clusters obtained by K-means and PCA analysis of the XANES spectra for all pixels (4 clusters in HZ-BD01 and 3 clusters in TGD-BD06). The average spectra of the clusters are shown in Figure 6d and 6f, respectively.

In HZ-BD01 (Figure 6a-d), Figure 6a shows a significant enrichment of iron in the pigment layer, with a small amount of iron beneath the glaze and pigment layers, indicating some degree of pigment dissolution. Figure 6b shows that iron in the pigment layer exists mainly in the form of Fe^{3+}. Less Fe^{2+} and more Fe^{3+} in the glaze layer and the layer under pigment. The Fe^{3+} distribution near the slip layer is uneven, indicating the presence of local redox non-uniformity at the micrometer scale within the layer. In Figure 6c, the K-means plot divides the entire measurement area into 4 clusters. The pigment layer, glaze layer, and the layer beneath the pigment each show only one cluster, indicating a similar iron environment within each layer. But the area near the slip layer contains two clusters, suggesting a greater variability in the iron environment. This is might due to interlayer reactions, which lead to greater variability in the local environment.

In TGD-BD06 (Figure 6e-h), the measurement area is acquired within the pigment layer. In the edge jump map, the red spots are enriched in Fe, the green area is the Fe-rich regions in the matrix, and the blue area correspond to Fe-poor regions (Figure 6e). Fe-rich particles contain higher levels of Fe^{3+}. The surrounding glass matrix has slightly lower levels of Fe^{3+} and higher levels of Fe^{2+}. All pixels were grouped into three clusters (Figure 6g), the average spectrum of cluster 1 is consistent with hematite. Clusters 2 and 3 have similar spectral shapes, but the absorption of cluster 3 is slightly higher at around 7120 eV, indicating that it is relatively more reduced (with a higher Fe^{2+} ratio), it corresponds to the Fe-poor matrix. This indicates micrometer-scale redox heterogeneity within the pigment layer, which may result from heterogeneous pigment dissolution and locally limited diffusion, together with spatial variations in oxygen fugacity during firing.

View Article Online
DOI: 10.1039/D6JA00035E

3.3 Fe speciation and distribution in pigmented areas

Figure 7 and Figure 8 show the results of the SIXES maps in the pigmented layers of TGD-BD14 and GZ-BD01, respectively. Two areas (area1 and area 2) were selected in each sample to observe the nature and the spatial distribution of Fe based crystals on the micrometer scale. Images showed in both figures are generated by calculating the differences in intensity of the Fe K-emission lines between energies corresponding to the main features of the reference spectra of iron-bearing oxides, which have been found in the pigmented area by Raman microscopy (Figure S3).

In TGD-BD14 (Figure 7), area 1 includes the glaze layer and pigment layer (Figure 7a), and area 2 includes the pigment layer and white slip (Figure 7b). By substracting the map collected at 7133 eV (feature B) from the map collected at 7131 eV (feature A), hematite (red area) and pseudobrookite (blue area) are highlighted positively and negatively, respectively. The results show that the pigment layer is dominated by hematite, which is widely distributed. Pseudobrookite occurs as large crystals but in small quantities. In the glaze layer, however, there is no iron-bearing crystals (Figure 7a). Iron-bearing particles are indeed restricted to the pigment layer and are rarely observed in the glaze or white slip, suggesting limited dissolution of the pigment and diffusion of ionic Fe into these layers, this might be attributed to the high Al content in the pigment, which acts as a refractory framework to increase local viscosity. As such, the decoration color is mainly controlled by the hematite in pigment layer.

In GZ-BD01 (Figure 8), the investigated areas are within the pigment layer. The reference models are hematite, pseudobrookite and ε-Fe_2O_3. Six energies (labeled A-F), corresponding to the most differences between the features of the reference spectra of hematite, pseudobrookite and ε-Fe_2O_3 are displayed in Figure 8h. Differences between maps were used to highlight specific phase distribution: B-A highlights hematite, C-E highlights ε-Fe_2O_3, and F-D highlights pseudobrookite. The distribution of hematite is shown in Figure 8a and 8e, ε-Fe_2O_3 is shown in Figure 8b and 8f, and pseudobrookite is shown in Figure 8c and 8g. Areas 1 and 2 both show that hematite occurs in larger sizes and greater abundance, whereas ε-Fe_2O_3 appears as smaller

View Article Online
DOI: 10.1039/D6JA00035E

spots distributed along hematite rims and more broadly within the glassy matrix. Pseudobrookite is only locally present and occurs as coarser grains. Within the pigment layer, hematite and ε-Fe_2O_3 constitute the dominant phases, consistent with an Fe^{3+}-rich environment.

3.3 Color mechanism of decorative patterns

The analytical results indicate that the pigments of the black and white porcelain are mainly composed of Fe^{3+}-bearing oxides, iron generally being in octahedral coordination in the structures. Hematite is the predominant crystal phase for the coloring formation.

At high temperatures, some hematite crystals diffused into the surrounding glass matrix and the overlying glaze. In these regions, iron is predominantly present as Fe^{3+} with a reduced coordination number, accompanied by a minor proportion of Fe^{2+}. Previous study proved that Fe^{3+} absorbs UV light regardless of whether it is in a tetrahedral or an octahedral environment [48]. Due to the deformation of the Fe ion coordination field, the absorption peak can expand and even reaches the visible light area, making the glass matrix appear brownish yellow [11]. Besides，Ti in the glassy matrix is predominantly present as Ti^{4+}, as shown in Figure S4, although Ti^{4+} itself is optically colorless, its high field strength and strong polarizing power can modify the local electric field and coordination symmetry around Fe^{3+}, thereby enhance the chromogenic capability of iron ions [49,50]. Therefore, the Fe-containing glassy matrix of the black and white porcelain sample appears brownish-yellow.

When the pigmented layer is thick and contains densely packed pigment particles, the particles will be the main contributing factor to the color of the patterns, giving them an opaque black color. When the pigment layer is thin, the glaze layer provides a more significant contribution in the coloring, giving the patterns a brown color. This explains why the patterns in the thinner areas and edges of the patterns appear brown, particularly in samples from the Xiangning (TGD) and Huozhou workshops (HZ).

The coloring mechanism of the black glaze in GZ01 differs from that of black and white porcelain, as it can be primarily attributed to Fe^{3+} ions

View Article Online
DOI: 10.1039/D6JA00035E

dispersed within the glaze layer instead of iron crystals. As such, when the glaze is relatively thin, a brownish tone is observed, whereas a thicker glaze absorbs more visible light, resulting in a darker appearance, up to black.

The decoration of TGD-BD04 is different from the others, as it displays a darker brown pigment near the upper glaze, and red layer below it, as shown in Figure 9a. μXRF-maps of the area highlighted by a red rectangle are shown in Figure 9b, both the brown and red areas are rich in iron (especially in crystals) and contain small amounts of K, along with some Ti-bearing particles. Figure 9c shows the average Fe K-edge XANES spectra collected in these two areas. Both spectra display the characteristic features of hematite. However, it is noteworthy that the hematite features appear significantly sharper in the spectrum of the red area than the one of the brown areas, suggesting that the Fe environment is closer to hematite in the red area. Further analysis of the pre-edge features, shown in Figure 9d, and the fitting results shown in Figure 9e, the red areas show a much higher t_{2g}/e_g ratio (0.99) than the brown areas (0.31). According to previous studies [51], the decrease in the t_{2g}/e_g ratio is usually associated with an increased degree of aberration in the coordination environment of the Fe^{3+} in octahedral site. Such structural distortion would induce a decrease in t_{2g}/e_g ratio, which leads to changes in the visible light absorption behavior. Specifically, a lower t_{2g}/e_g ratio shifts the absorption wavelength towards the long-wave direction and enhances the absorption of green and yellow light, giving a complementary purplish-black appearance, while an elevated ratio absorbs predominantly green-band light, giving a bright red color [51,52].

4 Conclusion

This study investigated six representative black and white porcelains alongside one black glazed ware produced by private workshops in southern Shanxi during the Jin dynasty. By investigating the morphology and valence state of iron using synchrotron-based X-ray absorption spectroscopy (μ-XANES), in combination with cross-sectional microstructural analysis of the decorated areas, this study provides new insights into the technological characteristics of black and white porcelain production and the color mechanisms of decorative patterns.

View Article Online
DOI: 10.1039/D6JA00035E

The production of black and white porcelain demonstrates a diverse range of raw material combinations. Pigments are derived from three main sources: iron-rich ores, iron-rich clays, and iron-rich glazes, while glazes can be categorized into Ca-rich and Ca-poor types based on the formation of anorthite. This flexible pairing of pigments and glazes is a typical trait of private workshops and reflects how different workshops utilized local resources. Besides, the technique of black and white porcelains is under-glazed decoration. During firing, significant elemental diffusion and interfacial reactions occur: calcium ions migrate from the glaze into the pigment layer, while iron ions diffuse from the pigment into the glassy matrix. This chemical evolution is not only a hallmark of high-temperature firing but also creates the distinct visual depth and strong interlayer bonding characteristic of black and white porcelain.

The μ-XRF and SIXES maps further revealed a targeted pairing strategy in our samples: highly fluid Ca-rich glazes are coupled with high-clay pigments, while viscous Ca-poor glazes are paired with iron-rich ores. This adjustment minimizes pigment dispersion at high temperatures, ensuring sharp black and white patterns. Such intentional material combinations reflect the craftsmen's profound understanding of raw material properties and their mastery in adapting techniques to materials.

The pre-edge feature of μXANES determined the average valence state and coordination of iron across the stratigraphy. Fe is present mostly as Fe^{3+} ions in an octahedrally coordinated environment, which indicates that the samples were fired in an oxidizing atmosphere, but the slight differences in oxidation levels between samples indicated variations in kiln atmosphere control.

The color of the black decorations results from the contributions of iron-bearing particles and the one of iron ions of the glass matrix. Due to the differences in the nature of Fe based crystals, their grain size and their concentration in black decorations, a variation in color tones and shades can be observed.

In conclusion, this study exemplifies the necessity to use synchrotron radiation-based micro-analyses to study the nature of this type of decoration. It not only allows an in-depth study of the valence and coordination of the

View Article Online
DOI: 10.1039/D6JA00035E

chromogenic elements, but also accurately reflects their chemical speciation and spatial distribution over relevant fields of view and with relevant spatial resolution. In particular, SIXES provides a practical and rapid approach for speciation mapping, as it allows to assess the spatial distribution of phases using only a few carefully selected energies.

Author contributions

Minli Wang: conceptualization, investigation, data acquisition, formal analysis, visualization, writing-original draft; Christophe Faulmann: formal analysis, methodology, validation, writing-review and editing; Clément Hole: data acquisition, software, writing-review and editing; data curation; Fen Wang: investigation, methodology; Chenchen Luo: formal analysis; Tian Wang: conceptualization, investigation, funding acquisition, resources; Philippe Sciau: supervision, project administration, conceptualization, methodology, writing-review and editing.

Acknowledgements

We acknowledge the European Synchrotron Radiation Facility (ESRF) for providing beam time at the ID21 beamline for the proposal number HG-226. In agreement to the ESRF data policy, the raw data related to this study can be found here: DOI10.15151/ESRF-ES-1306925003. This work was supported by the "Cultural Relics Scientific Identification and Research Innovation Team "project under the Shaanxi Province Sanqin Talents Special Support Program, the National Natural Science Foundation of China (No. U2574210, 52272019, and 52272020), the Central Government Guides Local Science and Technology Development Fund Project (No. 2024ZY-JCYJ-04–06), the Shaanxi Province Technology Innovation Guidance Special Project (No. 2024QY-SZX-04), and China Scholarship Council (CSC).

Reference

1 D. Qin, *Huaxia Archaeol.*, 2018, 58–74.

2 Z. Zhang, *Cizhou Kiln Porcelain Pillows*, People's Fine Arts Publishing House, Beijing, 2000.

3 F. Wang, *Pottery and porcelain of Yaozhou kiln*, Shaanxi University of Science and Technology Press, Shaanxi, 2000.

4 N. Wood, *Chinese glazes: their origins, chemistry and re-creation*, A. & C. Black, London, 2007.

5 D. Qin, *Cult. Relics*, 1994, **9**, 48–55.

6 S. Quartieri, M. Triscari, G. Sabatino, F. Boscherini and A. Sani, *Eur. J. Mineral.*, 2002, **14**, 749–756.

7 M. Wilke, F. Farges, P.-E. Petit, G. E. Brown and F. Martin, *Am. Mineral.*, 2001, **86**, 714–730.

8 L. Galoisy, G. Calas and M. A. Arrio, *Chem. Geol.*, 2001, **174**, 307–319.

9 F. Farges, Y. Lefrère, S. Rossano, A. Berthereau, G. Calas and G. E. Brown, *J. Non-Cryst. Solids*, 2004, **344**, 176–188.

10 F. Farges, S. Rossano, Y. Lefrre, M. Wilke and G. E. B. Jr., *Phys. Scr.*, 2005, 957.

11 V. Vercamer, G. Lelong, H. Hijiya, Y. Kondo, L. Galoisy and G. Calas, *J. Non-Cryst. Solids*, 2015, **428**, 138–145.

12 L. Bugaev, F. Farges, E. Rusakova, A. Sokolenko, Ya. Latokha and L. Avakyan, *Phys. Scr.*, 2005, 215.

13 M. Wilke, F. Farges, G. M. Partzsch, C. Schmidt and H. Behrens, *Am. Mineral.*, 2007, **92**, 44–56.

14 A. Bianconi, J. Garcia, A. Marcelli, M. Benfatto, C. R. Natoli and I. Davoli, *J. Phys. Colloq.*, 1985, **46**, C9-101-C9-106.

15 P. Sciau, Y. Leon, P. Goudeau, S. C. Fakra, S. Webb and A. Mehta, *J. Anal. At. Spectrom.*, 2011, **26**, 969.

16 M. Matsunaga and I. Nakai, *Archaeometry*, 2004, **46**, 103–114.

17 L. Lühl, B. Hesse, I. Mantouvalou, M. Wilke, S. Mahlkow, E. Aloupi-Siotis and B. Kanngiesser, *Anal. Chem.*, 2014, **86**, 6924–6930.

18 I. Cianchetta, K. Trentelman, M. S. Walton, J. Maish, A. Mehta and B. Foran, *J. Am. Ceram. Soc.*, 2016, **99**, 1792–1801.

19 A. Gianoncelli, G. Kourousias, S. Schöder, A. Santostefano, M. L'Héronde, G. Barone, P. Mazzoleni and S. Raneri, *Appl. Sci.*, 2021, **11**, 8052.

20 T. Wang, T. Zhu, Z. Feng, B. Fayard, E. Pouyet, M. Cotte, W. De Nolf, M. Salome and P. Sciau, *Anal. Chim. Acta*, 2016, **928**, 20–31.

21 R. Bugoi, B. Constantinescu, E. Pantos and D. Popovici, *Powder Diffr.*, 2008, **23**, 195–199.

22 L. Monico, K. Janssens, M. Cotte, S. M. Webb, F. Vanmeert, V. Gonzalez, G. Van Der Snickt, K. Keune, B. G. Brunetti, G. Falkenberg, J. Garrevoet, A. Van Loon, M. Vermeulen, M. Maguregui, S. De Meyer, E. A. Clerici, F. T. H. Broers, L. Cartechini, N. De Keyser, F. d'Acapito, F. Meirer, A. Romani, F. Rosi, S. C. Marri, D. Comelli, N. Deleu, I. Fazlic, M. Ghirardello, C. Holé, S. Pérez-Diez, M. Thoury and C. Miliani, *Riv. Nuovo Cimento*, 2025, **48**, 315–434.

23 M. S. D. Río, A. Sodo, S. G. Eeckhout, T. Neisius, P. Martinetto, E. Dooryhée and C. Reyes-Valerio, *Nucl. Instrum. Methods Phys. Res. Sect. B Beam Interact. Mater. At.*, 2005, **238**, 50–54.

24 G. Van der Snickt, J. Dik, M. Cotte, K. Janssens, J. Jaroszewicz, W. De Nolf, J. Groenewegen and L. Van der Loeff, *Anal. Chem.*, 2009, **81**, 2600–2610.

25 C. Holé, C. Dejoie, G. Wallez, Z. Ren, T. Wang and P. Sciau, *J. Phys. Chem. C*, 2025, **129**, 12150–12158.

26 F. Meirer, Y. Liu, E. Pouyet, B. Fayard, M. Cotte, C. Sanchez, J. C. Andrews, A. Mehta and P. Sciau, *J. Anal. At. Spectrom.*, 2013, **28**, 1870.

27 Y. Chen, R. Wen, L. Wang and M. Zhang, *Anal. Methods*, 2022, **14**, 541–548.

28 F. Gherardi, C. Hole, E. Campbell, M. Cotte, R. Tyson and S. Paynter, *J. Phys. Photonics*, 2024, **6**, 025001.

29 L. Wang and C. Wang, *J. Anal. At. Spectrom.*, 2011, **26**, 1796.

30 C. Xing, X. Deng, Y. Feng, L. Li, D. Chen, S. Chu, Y. Mu, L. Wu, L. Yan, L. Zhao, X. Feng, Y. Tao, Y. Li, S. Wu and G. Chang, *J. Eur. Ceram. Soc.*, 2025, **45**, 116892.

31 K. Sakurai, A. Iida, M. Takahashi and Y. Gohshi, *Jpn. J. Appl. Phys.*, 1988, **27**, L1768.

32 L. Monico, G. Van der Snickt, K. Janssens, W. De Nolf, C. Miliani, J. Verbeeck, H. Tian, H. Tan, J. Dik, M. Radepont and M. Cotte, *Anal. Chem.*, 2011, **83**, 1214–1223.

33 L. Monico, M. Cotte, F. Vanmeert, L. Amidani, K. Janssens, G. Nuyts, J. Garrevoet, G. Falkenberg, P. Glatzel, A. Romani and C. Miliani, *Anal. Chem.*, 2020, **92**, 14164–14173.

34 J. Demšar, T. Curk, A. Erjavec, Č. Gorup, T. Hočevar, M. Milutinovič, M. Možina, M. Polajnar, M. Toplak, A. Starič, M. Štajdohar, L. Umek, L. Žagar, J. Žbontar, M. Žitnik and B. Zupan, *J Mach Learn Res*, 2013, **14**, 2349–2353.

35 G. E. Brown Jr., F. Farges and G. Calas, in *Structure, Dynamics, and Properties of Silicate Melts*, eds J. F. Stebbins, P. F. McMillan and D. B. Dingwell, De Gruyter, 1995, pp. 317–410.

36 A. Fiege, P. Ruprecht, A. C. Simon, A. S. Bell, J. Göttlicher, M. Newville, T. Lanzirotti and G. Moore, *Am. Mineral.*, 2017, **102**, 369–380.

37 M. Wilke, G. M. Partzsch, R. Bernhardt and D. Lattard, *Chem. Geol.*, 2005, **213**, 71–87.

38 E. Cottrell, K. A. Kelley, A. Lanzirotti and R. A. Fischer, *Chem. Geol.*, 2009, **268**, 167–179.

39 V. A. Solé, E. Papillon, M. Cotte, Ph. Walter and J. Susini, *Spectrochim. Acta Part B At. Spectrosc.*, 2007, **62**, 63–68.

40 M. Wang, C. Faulmann, F. Wang, P. Sciau and T. Wang, *J. Raman Spectrosc.*

41 M. Wilke, C. Schmidt, F. Farges, V. Malavergne, L. Gautron, A. Simionovici, M. Hahn and P.-E. Petit, *Chem. Geol.*, 2006, **229**, 144–161.

42 M. Wilke, F. Farges, G. M. Partzsch, C. Schmidt and H. Behrens, *Am. Mineral.*, 2007, **92**, 44–56.

43 B. Hannoyer, M. Lenglet, J. Dürr and R. Cortes, *J. Non-Cryst. Solids*, 1992, **151**, 209.

44 P. A. Bingham, O. M. Hannant, N. Reeves-McLaren, M. C. Stennett and R. J. Hand, *J. Non-Cryst. Solids*, 2014, **387**, 47–56.

45 C. Holé, L. Leber, Q. Bruel, C. Muller, H. A. S. Orduz, T. Wang, P. Sciau and M. Cotte, *J. Am. Chem. Soc.*, 2025, **147**, 42433–42440.

46 C. Holé, Z. Ren, F. Wang, J. Zhu, T. Wang and P. Sciau, *Mater. Today Commun.*, 2022, **33**, 104329.

47 F. Wesenauer, C. Jordan, M. Azam, M. Harasek and F. Winter, *Materials*, 2021, **14**, 4942.

DOI: 10.1039/D6JA00035E

48 R. Kukkadapu, H. Li, G. Smith, J. Crum, J. Jeoung, W. Poisl and M. Weinberg, *J. Non-Cryst. Solids*, 2003, **317**, 301–318.

49 F. Farges and G. E. Brown, *Geochim. Cosmochim. Acta*, 1997, **61**, 1863–1870.

50 Y. Deng, Y. Zhou, Y. Yang, X. Shi, K. Zhang, P. Zhang and W. Yang, *Adv. Mater. Sci. Eng.*, 2018, **2018**, 5085031.

51 N. Nurdini, Moh. M. Ilmi, E. Maryanti, P. Setiawan, G. T. M. Kadja, and Ismunandar, *Heliyon*, 2022, **8**, e10377.

52 E. Maryanti, Moh. M. Ilmi, N. Nurdini, P. Setiawan, Y. M. Syah, C. Saiyasombat, G. T. M. Kadja, and Ismunandar, *Archaeol. Anthropol. Sci.*, 2022, **14**, 122.

View Article Online
DOI: 10.1039/D6JA00035E

Figures

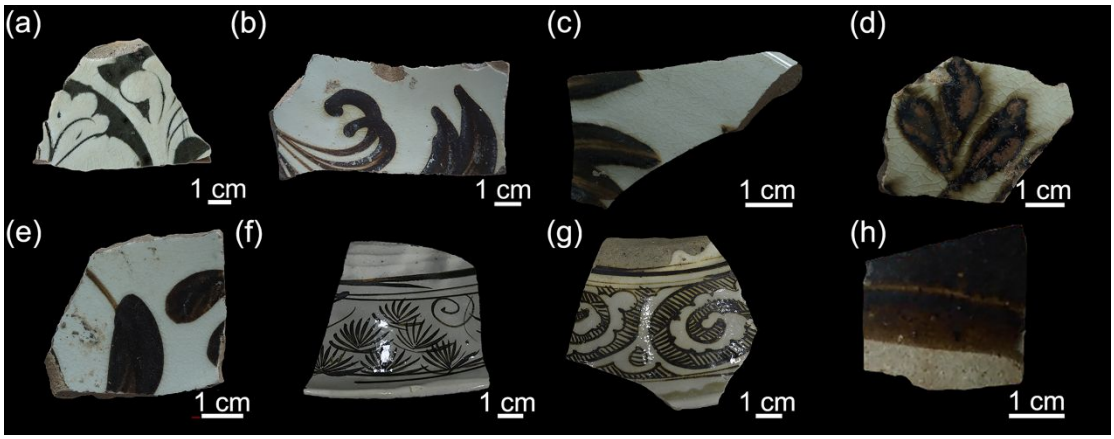

Figure 1 Photographs of the 8 studies sherds: (a) GZ-BD01; (b) TGD-BD04; (c) TGD-BD06; (d) TGD-BD08; (e) TGD-BD14; (f) HZ-BD01; (g) HZ-BD02; (h) GZ-01.

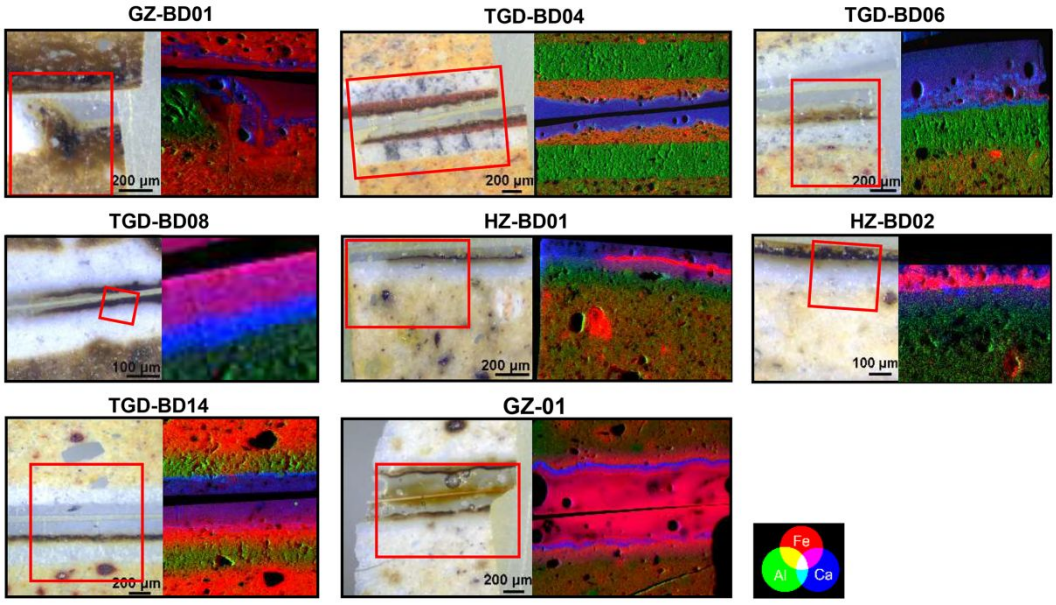

View Article Online
DOI: 10.1039/D6JA00035E

Figure 2 Samples differentiated by color in an optical microscopy image of a cross-sectional pigment area, and the distribution of Al, Ca, and Fe elements obtained in X-ray fluorescence mode.

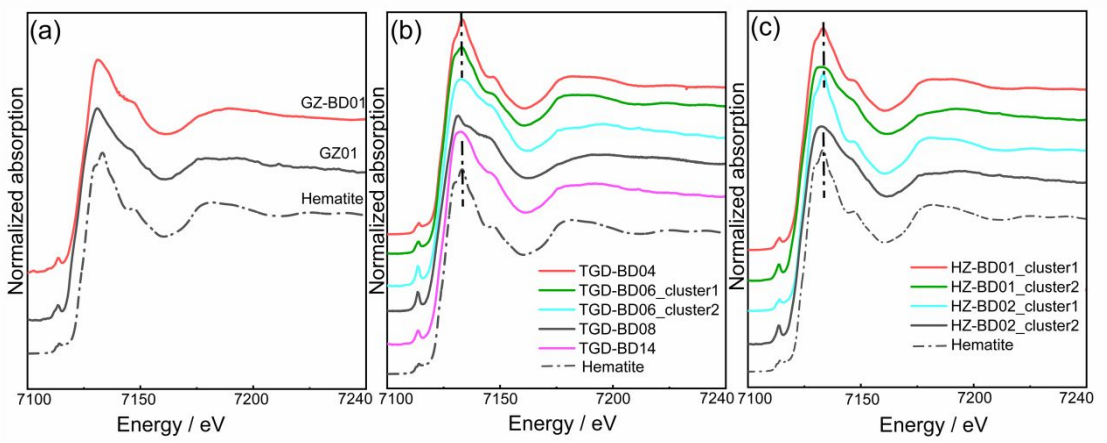

Figure 3 Average Fe XANES spectra of pigment area after PCA analysis: (a) GZ-BD01 and GZ-01; (b) TGD-BD04, TGD-BD06, TGD-BD08 and TGD-BD14; (c) HZ-BD01 and HZ-BD02.

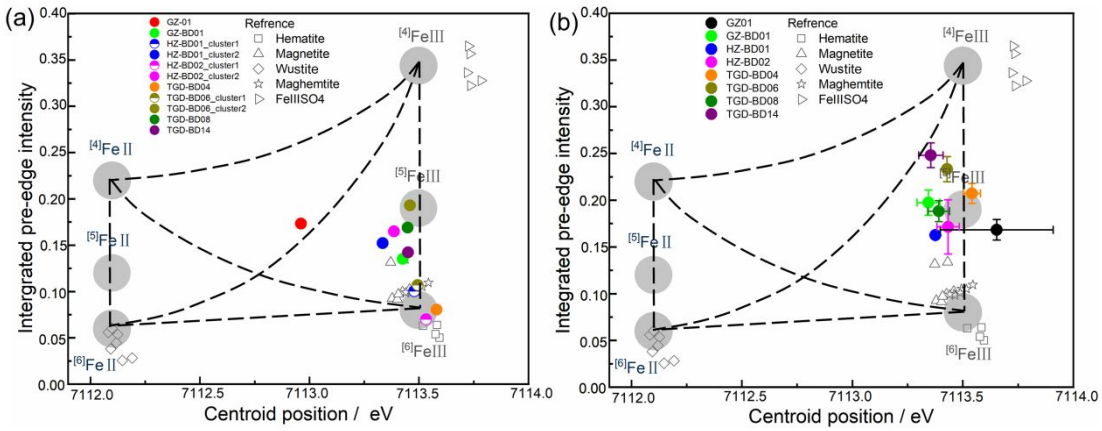

Figure 4 Scatter plot of the centroid and integrated intensity of the pre-edges of Fe XANES spectra of the (a) pigment area and (b) upper glaze.

Table 1 $Fe^{3+}/\Sigma Fe$ (%) average of each component of the samples obtained by pre-edge fitting and estimation.

Sample	GZ01 (black	TGD-BD08	HZ-BD01	HZ-BD02	TGD-BD04	GZ-BD01	TGD-BD06	TGD-BD14

View Article Online
DOI: 10.1039/D6JA00035E

Layers	glaze)							
Body	49.69	85.30	79.19	84.40	-	100*	90.99	100*
Pigment	49.01	77.64	82.52	81.41	100*	78.40	89.29	86.63
Glaze	100*	-	75.80	80.81	100*	72.17	83.03	70.92

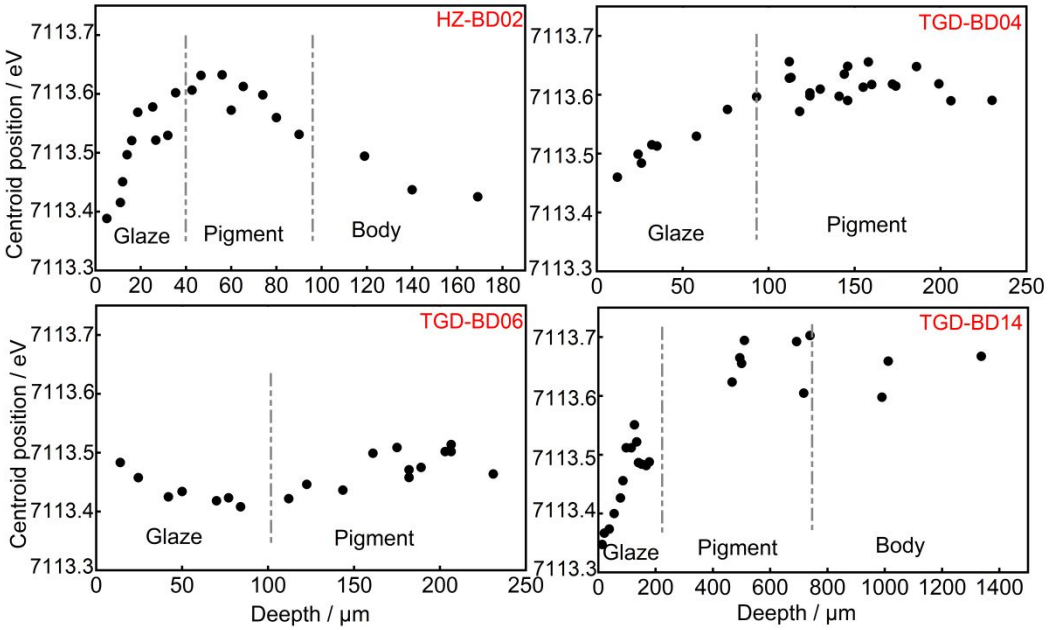

Figure 5 Scatter plot of the centroid position of pre-edges and the corresponding depth on cross section of HZ-BD02, TGD-BD04, TGD-BD06 and TGD-BD14.

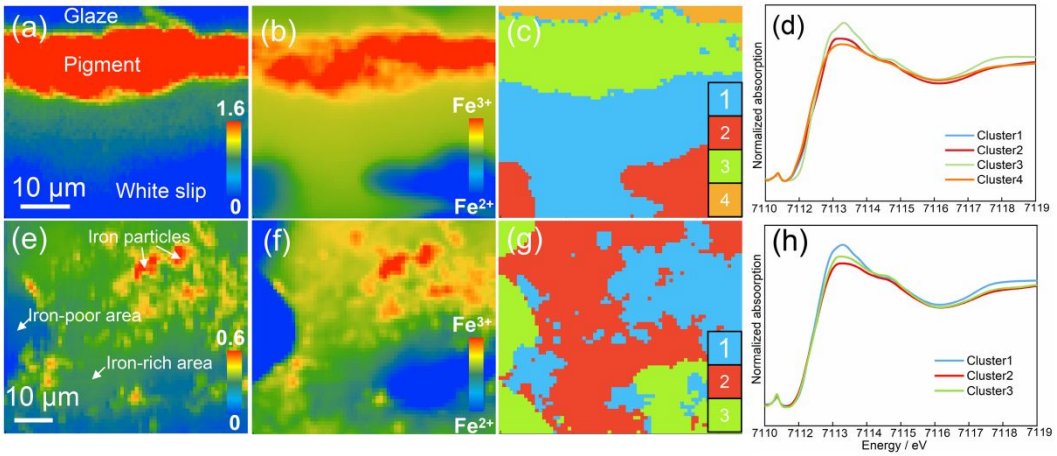

Figure 6 μ-XANES analysis of the Fe K edge of HZ-BD01 (a, b, c) and TGD-BD06 (e, f, g). (a, e) edge jumps (correlated to Fe concentration), (b, f) edge energy map at 7120 eV, the red region contains more Fe^{3+}, the blue region contains more Fe^{2+}. (c and d) the image segmentation obtained by

View Article Online
DOI: 10.1039/D6JA00035E

PCA and k-means clustering and (d and h) the corresponding average XANES spectra, 4 clusters in HZ-BD01 and 3 clusters in TGD-BD06.

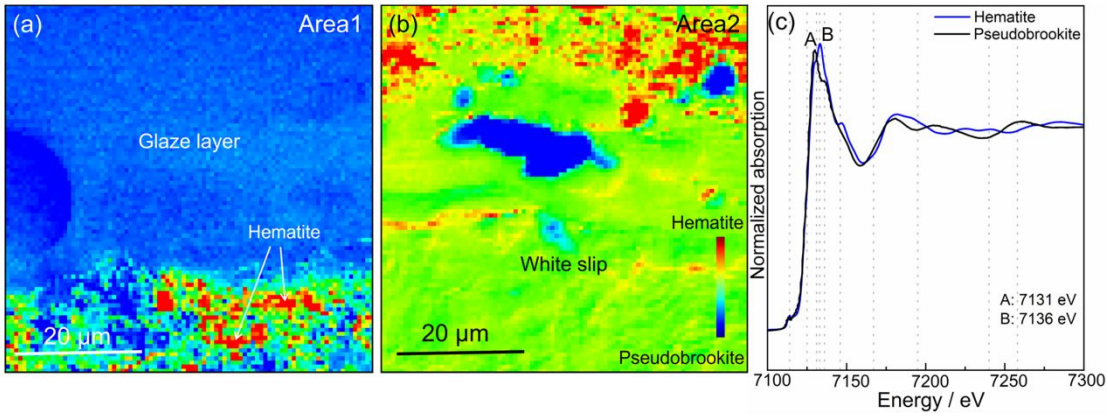

Figure 7 SIXES images of the (a) area1: glaze layer and pigment; (b) area2: pigment and white slip of TGD-BD14 acquired at multiple energies and stacked together. The reference spectra (c) are used to determine the differences in the spectra of hematite and pseudobrookite at certain energies. The differences between images acquired at 7133 eV (B) and at 7131 eV (A) highlight hematite positively (red) and pseudobrookite negatively (blue) in the pigment layer.

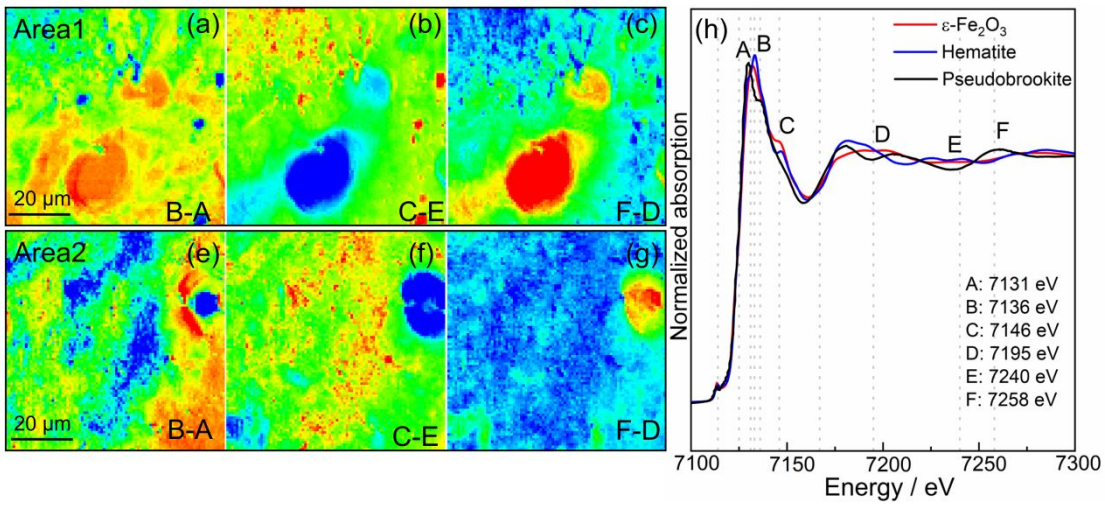

Figure 8 SIXES images of two pigment areas in GZ-BD01 (Area 1: panels a-c; Area 2: panels e-g). The reference spectra in (h) are used to determine the differences in the spectra of hematite, pseudobrookite and ε-Fe_2O_3 at

certain energies. (a and e) show the distribution of hematite by B-A, (b and f) highlight the distribution of ε-Fe_2O_3; (c and g) show of pseudobrookite by F-D.

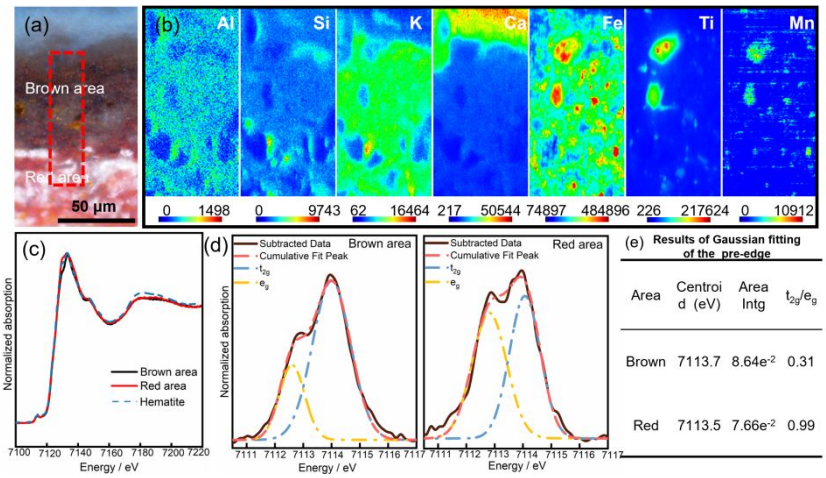

Figure 9 (a) Cross-sectional optical micrograph of TGD-BD04 showing the red and brown areas; (b) XRF-map of the area outlined in red in (a); (c) Fe K-edge XANES spectra acquired from the red and brown areas, respectively; (d) Pre-edge fitting results of brown area (left) and red area (right); (e) Results of Gaussian function fitting of the pre-edge.

View Article Online
DOI: 10.1039/D6JA00035E

Data Availability Statement:

All primary data supporting the findings of this study, including processed μ-XRF maps, μ-XANES spectra and maps, and microstructural images, are available within the article and its electronic supplementary information (ESI). The raw synchrotron datasets are available from the ESRF data repository at https://doi.esrf.fr/10.15151/ESRF-ES-1306925003.